Journal of Molecular Structure 1149 (2017) 862–873

Contents lists available at ScienceDirect

Journal of Molecular Structure

journal homepage: http://www.elsevier.com/locate/molstruc

Synthesis, spectroscopic and photophysical studies of xanthene derivatives

Mohammad Ramezani Taghartapeh [a, *], Nader Noroozi Pesyan [a], Hamid Rashidnejad [a], Hamid Reza Khavasi [b], Alireza Soltani [c]

[a] Department of Organic Chemistry, Faculty of Chemistry, Urmia University, 57159, Urmia, Iran
[b] Department of Chemistry, Faculty of Science, Shahid Beheshti University, Tehran, Iran
[c] Joints, Bones and Connective Tissue Research Center, Golestan University of Medical Science, Gorgan, Iran

ARTICLE INFO

Article history:
Received 19 June 2017
Received in revised form
10 August 2017
Accepted 15 August 2017
Available online 18 August 2017

Keywords:
Xanthene
Hirshfeld surface analysis
Spectroscopic analysis
DFT and TD-DFT calculations
Non-liner optical parameters

ABSTRACT

We report on the experimental, crystal structure and computational investigation of a new class of xanthenes obtained by the reaction of salicylaldehyde and its derivatives with, 5,5-Dimethylcyclohexane-1,3-dione (Dimedone). The synthesized xanthenes were characterized by state-of-the-art techniques, such as IR, Raman, ^{1}H and ^{13}C NMR, Single Crystal X-ray crystallography, UV–Vis and photophysical measurements. The structure, ground- and excited-state properties of one xanthene derivative was investigated using Density Functional Theory (DFT) and Time-Dependent DFT (TD-DFT) calculations with and without solvent (ethanol). The optimized geometries and predicted IR frequencies were in good agreement with experimental data. Hirshfeld surface analyses were carried out to gain insight on the close-contact interactions of the crystal, where hydrogen showed the highest contribution (66.1%). The synthetic route proposed in this work does not use any catalysts and leads to high yields (75–85%), therefore being an interesting alternative to synthesize xanthene derivatives.

1. Introduction

The chemistry of xanthene derivatives with their countless applications has attracted the attention of synthetic pharmacologists, laser physicists, and chemists [1]. Many applications in biology and photochemistry have been reported utilizing these compounds as anti-viral, anti-inflammatory and anti-bacterial agent [2–6]. These molecules have also been used as dyes in laser technology and as pH-sensitive fluorescent materials for bio-imaging [7,8]. Moreover, they exhibit potential cytotoxic activity against colon cancer cell lines, especially for Colon-205 and Colon-502713 [9]. Some xanthene-based drugs were efficiently intercalated into the DNA and also have been reported to act as radical scavengers [10,11].

Xanthene dyes can be synthesized by means of a catalytic reaction using $(PhCO_2)_2$, Friedel–Crafts reaction, application of DABCO or using salicylaldehyde [12–15] among others [16]. In view of the very large variety of xanthene derivatives and their even larger range of applications, the development of novel synthetic protocols to obtain different xanthene molecules is very important. The understanding of alternative reactions in the synthesis of xanthenes and its derivatives is therefore a key factor, if one wishes to generate novel drugs, dyes and materials with promising properties.

Theoretical methods can help elucidate synthetic mechanisms of xanthene, as well as to characterize the final product by means of predicting several ground- and excited-state properties. The use of such methods is often seen in different fields of science, such as chemistry, physics, and biology [17–21] In particular, Density Functional Theory (DFT) and Time-Dependent DFT (TD-DFT) have been broadly employed in many experimental-theoretical investigations [22–24], which is due to the simplicity and predictive power of these methods when compared with computationally more demanding *ab initio* methods. Among the many different DFT methods developed so far, the hybrid B3LYP functional has been extensively used to treat organic molecules [23,24], which is due to its low computational cost when compared with other functionals, associated to a high accuracy in the prediction of general properties of those molecules.

In this work we present an alternative synthetic method to obtain new xanthene derivatives and make their characterization

* Corresponding author.
E-mail address: mramezanitaghartapeh@swin.edu.au (M.R. Taghartapeh).

http://dx.doi.org/10.1016/j.molstruc.2017.08.054
0022-2860/

by means of combining several experimental techniques and further DFT and TD-DFT calculations over 9-(2-hydroxy-4,4-dimethyl-6-oxocyclohex-1-enyl)-3,3-dimethyl-2,3,4,9-tetrahydro-1*H*-xanthen-1-one (**6**). It has a potential application for use as a selective and orally active antagonist for neuropeptide YY5 receptor (xanthene class of Y5 antagonists) [3]. It was previously synthesized using alkali [25], acetic acid/H_2O [26], and water catalyzed by triethylbenzylammonium chloride [27] We show that our alternative synthetic protocol not only gives comparable yields as those reported in the literature for **6**, but also is considerably cheaper and does not use any catalysts.

2. Methodologies

2.1. Synthesis

The condensation reaction of 5, 5-dimethylcyclohexane-1, 3-dione (dimedone, compound **1**) with salicylaldehyde (**2**) and its derivatives (**3**–**5**) in EtOH under reflux afforded the xanthene class of derivatives (**6**–**9**, See Schemes 1 and 2) based on the mechanism represented as Scheme 1. Dimedone (10 mmol, 1.4 g) and salicylaldehyde (5 mmol, 0.6 g) were dissolved in 20 ml ethanol, stirred in a round bottom flask for 24 h, precipitated, filtered off, then washed with cold ethanol to yield a white solid (**6**). A similar procedure was used to synthesize **7**–**9**. All reactions were monitored by TLC with silica gel-coated plates (AcOEt:AcOH/80:20/v:v). Compounds **1** and **2** and all solvents used in this work were purchased from Merck and Aldrich, without further purification. Single crystal of **6** was obtained as a colorless crystal by slow evaporation of the solvent (EtOH) at room temperature.

2.2. Characterization

Products 6–9 were characterized using state-of-the-art techniques. Melting points were measured with a digital melting point apparatus (Electrothermal), (Urmia University, Urmia, Iran). IR spectra were recorded in the region 4000–400 cm^{-1} on a NEXUS 670 FT-IR spectrometer (resolution: 0.1 cm^{-1}) by preparing KBr pellets (Urmia University, Urmia, Iran). Raman spectrum was recorded in the region 100–4400 (cm^{-1}) using Teksan Spectroscopy (Model: Takram P50C0R10) that has the resolution of 0.6 cm^{-1}. The 1H and 13C NMR spectra were recorded on a high-resolution Bruker 300 FT-NMR at 300 and 75 MHz, respectively (Urmia University, Urmia, Iran). 1H and 13C NMR spectra were obtained in CDCl3 using TMS as internal standard and elemental analysis (CHN), just for **6,** was also performed (Urmia University, Urmia, Iran). The UV–visible spectrum of 6 was recorded on a T80 UV–Vis spectrometer (PG Instruments Ltd) in the region 190–1100 nm with the resolution of 0.2 nm and the photoluminescence spectra of **6** at room temperature and different concentrations were carried out using a Jasco 6500 spectrophotometer with a xenon lamp and 1 nm of resolution bothat (Urmia University, Urmia, Iran). Single crystal X-ray diffraction of 6 was also collected on STOE IPDS-II or IPDS-2T (Shahid Beheshti University, Tehran, Iran) with the detector resolution of 0.15 mm pixels mm^{-1}.

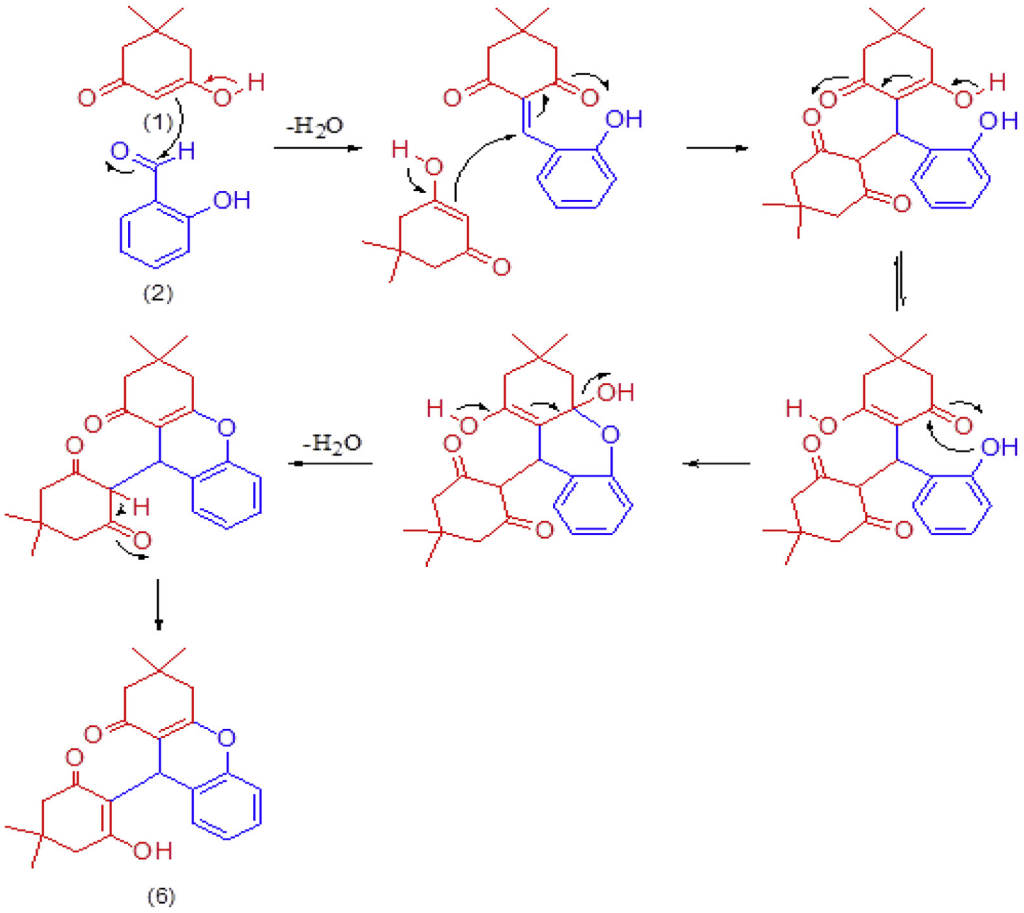

Scheme 1. Proposed mechanism for the formation of **6**–**9**.

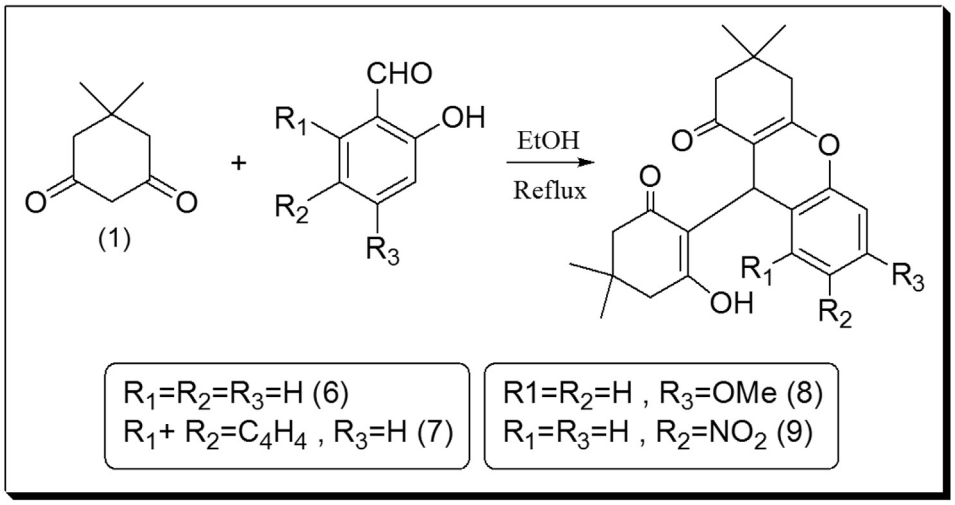

Scheme 2. Schematic reactions for the formation of **6**–**9**.

2.3. Theoretical calculations

The geometry of **6** was optimized using DFT calculations with the hybrid (B3LYP) and non-hybrid (PBE0) functionals and 6−311++G** basis set using the Gaussian 09 program package [28]. Solvent effects were included in the calculations via the PCM model, where the dielectric constant of ethanol ($\varepsilon = 24.852$) was used. Vibrational frequencies were also calculated at PBE1PBE and B3LYP functionals and 6−311++G** basis set to check the reliability of the optimized structure, as well as to help assign experimental IR transitions with further studies of all possible vibrational assignments using VEDA software [29]. TD-DFT was then employed to predict the excited states of **6** using the previously optimized ground state geometry with the same functional and basis set. The oscillator strengths and intensities of each transition were used to build a theoretical UV−Vis spectrum, where Gaussian functions with fixed widths were centered at each transition wavelength.

2.4. Hirshfeld surface analysis

In order to discuss the packing of **6** inside the molecular crystal, as well as to discuss the close contacts between atoms in the single crystal in solid, a Hirshfeld analysis was carried out. A detailed analysis was carried out to study various intermolecular interactions of H···H, H···O/O···H, C···H/H···O and O···O types of contacts present in the crystal structures of **6**, using the program Crystal Explorer 3.0 [30].

3. Results and discussion

3.1. Appearance, melting point value and interpretation of FT-IR, H NMR and C NMR of *6*–*9*

9-(2-Hydroxy-4,4-dimethyl-6-oxocyclohex-1-enyl)-3,3-dimethyl-2,3,4,9-tetrahydro-1H-xanthen- 1-one(**6**): White solid; m.p. 191−193 °C (decomps.); FT-IR (KBr) 3180.8 (OH), 2953.9, 2927.6, 2869.3 (CH aliph.), 1642.3 (C=O), 1593.4 (C=C ar.), 1374.1 (CH3), 1232.2 (C−O) cm^{-1}; 1H NMR (CDCl3, 300 MHz) δ 1.01 (s, 6H), 1.04 (s, 3H), 1.14 (s, 3H), 1.97 (d, 2H, $J = 4.8$ Hz), 2.33−2.59 (m, 6H), 4.68 (s, 1H), 7.05−7.18 (m, 4H), 10.48 (bs, 1H); 13C NMR (CDCl3, 75 MHz) δ 200.9196.5, 170.7, 169.1, 151.1, 128.0, 127.5, 124.6, 124.3, 118.3, 115.7, 111.1, 50.6, 49.9, 43.2, 41.6,32.3, 30.9, 29.9, 29.2, 27.8, 27.2, 26.5. (Supplementary Information section, Figs. S1−6).

Elemental analysis of (**6**): $C_{23}H_{26}O_4$, Calc.: C 75.5%, H 7.1%. found: 77.2%, H 7.2%.

12-(2-Hydroxy-4,4-dimethyl-6-oxocyclohex-1-enyl)-9,9-dimethyl-9,10-dihydro-8Hbenzo[a]xanthen-11(12H)-one (**7**): White solid; m.p. 243 °C (decomps.); FT-IR (KBr) 3173.4(OH), 2944.9 (CH aliph.), 1642.5 (C=O), 1591.6 (C=C ar.), 1374.7 (CH3), 1236.0 (C−O) cm^{-1}; 1H NMR (CDCl3, 300 MHz) δ 0.72 (s, 3H), 0.94 (s, 3H), 1.06 (s, 3H), 1.16 (s, 3H), 1.82 (d, 1H,$J = 15.3$ Hz), 1.95 (d, 1H, $J = 15.3$ Hz), 2.39 (m, 4H), 2.55 (d, 1H, $J = 17.4$ Hz), 2.67 (d, 1H, $J = 17.4$ Hz), 5.26 (s, 1H), 7.25−7.70 (m, 6H), 10.67 (bs, 1H); 13C NMR (CDCl3, 75 MHz) δ 201.0,196.8, 170.2, 169.0, 148.9, 131.3, 131.0, 128.5, 128.4, 126.7, 124.6, 122.9, 117.7, 116.6, 116.1111.1, 50.7, 50.0, 43.2, 41.4, 32.4, 30.6, 29.8, 29.3, 27.1, 26.4, 25.4.

9-(2-Hydroxy-4,4-dimethyl-6-oxocyclohex-1-en-1-yl)-5-methoxy-3,3-dimethyl-2,3,4,9-tetrahydro-1H-xanthen-1-one (**8**): White solid; White solid; m.p. 202−205 °C (decomps.); FT-IR (KBr) 3202(OH), 3029 (CH ar.), 2954 (CH aliph.), 1643 (C=O), 1586 (C=C ar.), 1376 (CH3), 1229 (C−O)cm^{-1}; 1H NMR (CDCl3, 300 MHz) δ 1.01 (s, 6H), 1.04 (s, 3H), 1.13 (s, 3H), 1.98 (d, 2H, $J = 4.8$ Hz), 2.34−2.72 (m, 6H), 3.90 (s, 3H), 4.68 (s, 1H), 6.60 (d, 1H, $J = 7.5$ Hz), 6.77 (d, 1H, $J = 8.1$ Hz), 6.95 (t, 1H, $J = 7.8$ Hz), 10.43 (bs, 1H); 13C NMR (CDCl3, 75 MHz) δ 200.9, 196.5, 170.6168.8, 147.1, 140.7, 125.2, 124.2, 119.8, 118.2, 110.9, 110.4, 56.1, 50.6, 50.0, 43.2, 41.6, 32.3,30.9, 29.9, 29.1, 27.8, 27.2, 26.5.(Supplementary Information section, Figs. S7−11).

9-(2-Hydroxy-4,4-dimethyl-6-oxocyclohex-1-en-1-yl)-3,3-dimethyl-7-nitro-2,3,4,9-tetrahydro-1H-xanthen-1-one (**9**): White solid; m.p. 206−208 °C; FT-IR (KBr) 3184 (OH), 2958 (CH aliph.), 1652 (C=O), 1597 (C=C ar.), 1376 (CH3), 1239 (C−O) cm^{-1}; 1H NMR (CDCl3, 300 MHz) δ 0.96 (s, 6H), 1.03 (s, 3H), 1.15 (s, 3H), 1.98 (m, 2H), 2.36−2.65 (m, 6H), 4.70 (s, 1H), 7.12 (d, 1H, $J = 9.0$ Hz), 7.93 (d, 1H, $J = 2.1$ Hz), 8.05 (dd, 1H, $J = 8.7$, 2.4 Hz), 10.34 (bs, 1H); 13C NMR(CDCl3, 75 MHz) δ 200.8, 196.9, 172.0, 167.8, 155.4, 144.2, 125.9, 123.8, 123.6, 117.6, 116.4110.9, 50.5, 49.9, 43.2, 41.2, 32.3, 31.2, 29.6, 29.2, 27.8, 27.0, 26.7. (Supplementary Information section, Figs. S12−16).

Compounds **6**–**9** were obtained with high yields: 85%, 75%, 82%, and 84%, respectively. These results are very good, especially if one remembers that no catalysts were used in the reactions. The compound **6** was chosen as a representative compound to be further investigated with X-Ray measurements and Hirshfeld surface analysis, as well as with theoretical DFT and TD-DFT calculations.

3.2. Crystal structure, theoretical intermolecular H-bonds and theoretical pKa analysis of **6**

The crystallographic structure of **6** was elucidated using X-ray diffraction of the single crystal (Supplementary Information section, Fig. S20). This compound crystallizes in the monoclinic space group $P2_1/c$. The relevant data is represented as a summary in Table 1. Boat and half-chair conformations were observed for the main pyran and outer cyclohexene of the xanthene moiety, respectively. As reported in the literature, there is other cyclohexane with skew boat conformation that is bonded to the central pyran [27].

The crystal structure of **6** indicates three kinds of H-bonds. Intermolecular H-bonds were observed between H2B and O3 (Fig. 1 right), where donor–acceptor distances d (O···O) were 2.664 Å. This value falls within the range 2.5 ≤ d (O···O) ≤ 2.7 Å, which is typical for medium strong H-bonds [31–34]. Values for d (O···O) of two other H-bonds indicate these bonds are weak, as shown in (Table 2).

Further study of the H-bonds strength in **6** and consequent comparisons with those of other carboxylic and flavones acids and methyl 2,4-dimethoxysalicilate reported by Wallet et al. [35,36]and Dabbagh et al. [37], have permitted us to elucidate the pKa of **6** when the experimental quantification of pKa is difficult. The estimated pKa value for intermolecular H-bond of **6** is ≈ 5.6 which is in good agreement with the experimental results for xanthene class of compounds (Fluorescein = 6.10 ± 0.04 and 2-(3, 6- dihydroxy-9-acridinyl) benzoic acid–azafluorescein = 6.23 ± 0.0.9) reported by Batistela and coworkers [38]. Moreover, based on the correlation between H-bond strength (E_{HB}) and d (O···O) [37,39], one can find E_{HB} ≈ 21 kcal mol^{-1} for **6** (Supplementary Information section, Figure S21).

3.3. Hirshfeld surface analysis (HSA) of **6**

HSA was carried out to understand and better describe the crystal packing of **6**, where close contacts can be easily highlighted. Two-dimensional fingerprint plots were used to quantify and visualize the intermolecular interactions involved in this packing, which are shown in Fig. 2. The Hirshfeld surfaces were constructed using different representations, such as d_e, d_i,d_{norm} [40], shape index and curvedness. In the Hirshfeld surface diagrams, the close contacts whose distances are equal to the sum of the van der Waals radius of both close-contact atoms are white colored, while the close contacts whose distances are shorter than and longer than that sum are represented by red and blue, respectively. Any part of every fingerprint represents a close contact, which is highlighted in Blue (Fig. 2i–m). The total percentile contributions of close contacts such as H···H, O···H/H···O, C···H/H···C, and O···O were 66.1%, 18.5%, 14.2% and 1.2%, respectively. As one can see, the intermolecular H···H contact share predominant in the packing of **6**.

Table 1
Crystal data for 9-(2-hydroxy-4,4-dimethyl-6-oxocyclohex-1-enyl)-3,3,dimethyl-2,3,4,9-tetrahydro-1H-xanthen-1-one.

Crystal data	
Formula structure	$C_{23}H_{26}O_4$
M_r	366.44
Crystal system, space group	Monoclinic, $P2_1/c$
a	7.0527 (9) Å
b	20.295 (2) Å
c	13.682 (2) Å
α	90°
β	93.295 (12)°
γ	90°
V	1955.1 (5) Å^3
Z	4
Mo $K\alpha$ radiation, λ	0.71073 Å
μ	0.08 mm^{-1}
T	298 K
Crystal dimension	0.22 × 0.20 × 0.15 mm
R_{int}	0.145
$R[F^2 > 2\sigma(F^2)]$	0.102
w$R(F^2)$	0.185
S	1.17
$\Delta\rho_{max}$	0.19 e Å^{-3}
$\Delta\rho_{min}$	−0.19 e Å^{-3}
Measured reflections	22118
Independent reflections	5297

3.4. Geometry optimization of **6**

The geometry of **6**was optimized using DFT calculations (Fig. 3) indicate that there are negligible changes within the bond length, bond angle, and torsion angle values obtained by crystal structure and those calculated at B3LYP method. Comparative data of theoretical and experimental geometrical parameters are presented in (See Supplementary Information section, Table S1). The predicted bond lengths, bond angle and torsion angles. for **6** in both vacuum and ethanol phases as solvent were in good agreement with the crystallographic results revealing the reliability of the B3LYP and PBE0 methods for optimizing the geometry of xanthene class of compounds, as already reported in several previous reports [18–21,41]. There may be some differences and that are mainly due to the unimolecular gas phase optimization for the former, where intermolecular interactions do not exist [40].

3.5. Experimental and calculated absorption and emission spectra of **6**

The absorption and emission spectra of 6 in ethanol at room temperature are shown in Fig. 4 (Blue and red lines). This emission spectrum was also measured for different concentrations (2.2×10^{-3} M, 1.1×10^{-3} M, and 5.5×10^{-4} M) and did not show any changes in shape whereas the intensity of the emission spectra increased upon the lowing of the concentration of**6**. (Supplementary Information section, Fig. S22**)**. Both absorption and emission occur mostly at the UV region and its molar absorptivity in ethanol at λ_{max} (280 nm) is 2×103 M^{-1} cm^{-1}, which is low when compared with other xanthenes, while the λ_{em} has emerged at 340 nm resulting in a Stokes shift (Δλ) of 60 nm as the consequences of no symmetry and moderate value of dipole moment to the long axes of **6**, the fluorescence band moderately overlaps the absorption band (Fig. 4) [42], makes it a promising candidate for bio-imaging and bio-diagnostics applications [43]. This value appreciably corresponds toΔλ of a xanthene dye reported by Yang et al. [44]. The theoretical absorption spectrum is in good agreement with the experimental one, the deviation found being attributed to the implicit solvent model (PCM) used instead of the computationally-demanding explicit model, as well as to limitations on the basis set and functional used. The PBE0 functional gave considerably better results than B3LYP for the excited states of 6 when compared with experimental values (Fig. 5).

For all ground-state properties we used B3LYP and PBE0 functionals, while the B3LYP converges much faster than PBE0 and has similar accuracy. The compositions of the electronic transitions in terms of molecular orbitals are shown in Table 3. The maximum absorption occurs at 300 nm and corresponds to

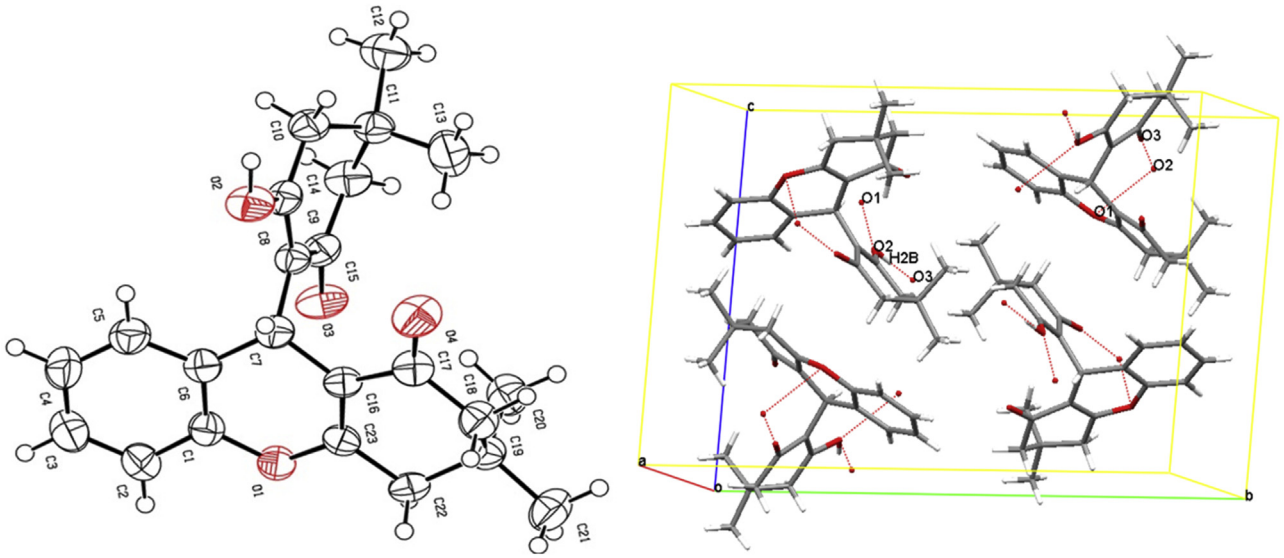

Fig. 1. ORTEP diagram (left) and respective crystal packing showing intermolecular oxygen-oxygen close contacts (right) of 9-(2-hydroxy-4,4-dimethyl-6-oxocyclohex-1-enyl)-3,3,dimethyl-2,3,4,9-tetrahydro-1*H*-xanthen-1-one.

Table 2
Intermolecular H-bond distances (Å) and angles (degree) for 9-(2-hydroxy-4,4-dimethyl-6-oxocyclohex-1-enyl)-3,3,dimethyl-2,3,4,9-tetrahydro-1*H*-xanthen-1-one.

D–H···*A*	*D*–H	H···*A*	*D*···*A*	*D*–H···*A*	Strength
O2–H2*B*···O3^{i}	0.89 (4)	1.80 (4)	2.664 (3)	165 (4)	Medium Strong
C7–H7···O2	0.98	2.33	2.793 (4)	108	Weak
C20–H20*B*···O4^{ii}	0.96	2.58	3.433 (4)	148	Very weak

Symmetry codes: (i) x+1, y, z; (ii) x−1, y, z.

the π → π* electronic transition from the highest-occupied molecular orbital (HOMO) to the lowest unoccupied molecular orbital (LUMO), as well as from HOMO to LUMO+1 almost in all calculated cases. Concerning the literature for the absorption of xanthene dyes, our results agree well with the λ_{max} reported for some xanthene dyes synthesized using aldehydes (dibenzo[*b*, *d*] furan-2-carbaldehyde, dibenzo[*b*, *d*] thiophene-2-carbaldehyde and 9-methyl-9*H*carbazole-3-carbaldehyde) and cyclic 1,3-dicarbonyls which were in the range of 285 nm–302 nm obtained in three different solvents (Chloroform, acetonitrile and tetrahydrofuran) [45]. The second major peak is observed between 309 and 325 for the studied states which mainly corresponds to H-1 → L and finally the third main peak of the studied states were observed in the range of 325–345 with the π → π* electronic transition from H → L and an exception of H → L+1 (38%) as the major contribution in PBE0 (Ethanol) model of transition state calculation. The main occurred electronic transition can be attributed to n → π* transitions due to the possible conjugations of lone pair of hydroxyl and Ketone functionalities with the *β*double bonds ($C_{15} = C_{17}$ and C_8═C_9) and also the lone pair of O atom of pyran ring that has resonance with the electrons of π bonds of benzene ring of **6**. Moreover, Tables 3 and 4 represent that the λ_{max} at both B3LYP and PBE functionals reduced from vacuum to ethanol phase resulted in more stabilization of n transition which consequently reduces the E_{gap} of **6**.

3.6. Electronic properties of **6**

The calculated electron density of the frontier molecular orbitals (FMOs) of **6** in vacuum and ethanol calculated at B3LYP/6–311++G** functional is plotted in Fig. 6 and their energies are summarized in Table 4. The energies of HOMO and LUMO were determined to be (−5.92 and −1.44 eV for vacuum phase) and (−5.80 and −1.28 eV for ethanol phase) with the corresponding E_{gap} of 4.48 and 4.52 eV, respectively. Moghanian et al. stated that the HOMO, LUMO and E_{gap} calculated for the synthesized xanthene were −5.57, −1.19 and 4.38 eV, which appreciably confirm our calculated results [46]. Moreover, recently K. Anandhan et al. reported a similar data for these items that were −5.52, −1.19 and 4.38 eV, respectively. Fig. 6 clearly shows that the HOMO is delocalized over the aromatic moiety of the molecule and has a large contribution from the oxygen atoms. Using the Koopmans' theorem [47,48] and calculated values of HOMO and LUMO, we determined quantum molecular descriptors of chemical potential (μ), global hardness (η), electrophilicity index (ω), and softness (S) in the gas and solvent (ethanol) phases, respectively, whose values are shown in Table 4.

The molecular orbitals calculated for **6** were used to make the Molecular Electrostatic Potential (MEP) plot, from where regions of positive and negative potentials can be seen (Supplementary Information section, Fig. S23). Mulliken atomic partial charges were also calculated for **6** in vacuum and in ethanol (Supplementary Information section, Table S2). Both results predict the most negative region of **6** to be located around the carbonyl group while the outer ring of that compound, which bears the hydroxyl group, is related to a more positive region. The Molecular Electrostatic Potential (MEP) map is a very practical three-dimensional diagram which reveals features of the electronegativity and electropositivity of molecular structures. MEP maps are a valuable tool in organic chemistry to predict the behavior of complex molecules [47,48] The MEP plot of compound **6** is shown in Fig. S4. Blue and red zones represent positive and negative potentials, respectively. The increase of negative electronic potential can be observed by the color changes, as blue (more positive) <green < yellow < orange < red (more negative) [49,50]. As it is

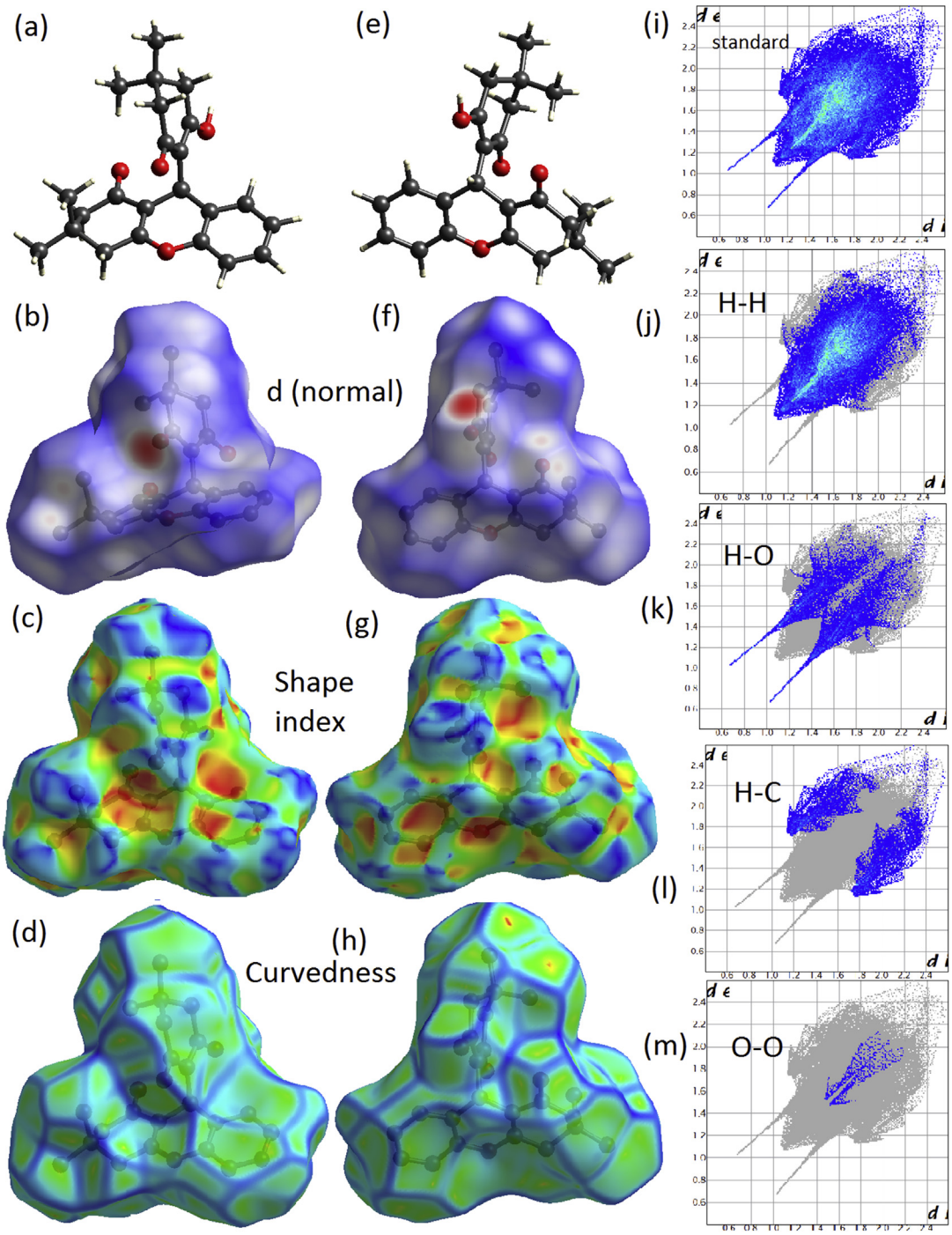

Fig. 2. (a–h): Views of the Hirshfeld surfaces mapped with d_{norm}, shape index and curvedness viewed from front (a–d) and back (e–h) faces and 2D fingerprint plots for 6 with different close contacts and their relative contributions (i–m) of 9-(2-hydroxy-4,4-dimethyl-6-oxocyclohex-1-enyl)-3,3,dimethyl-2,3,4,9-tetrahydro-1*H*-xanthen-1-one.

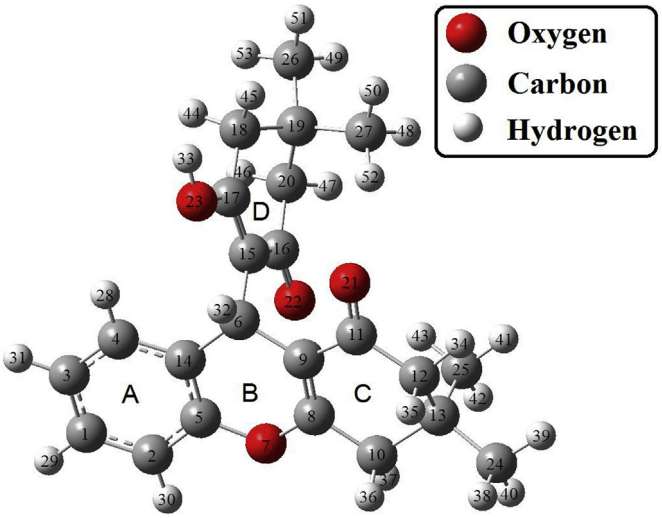

Fig. 3. Optimized structure of 9-(2-hydroxy-4,4-dimethyl-6-oxocyclohex-1-enyl)-3,3,dimethyl-2,3,4,9-tetrahydro-1H-xanthen-1-one labeled according to the number of atoms and the rings named as A, B, C and D.

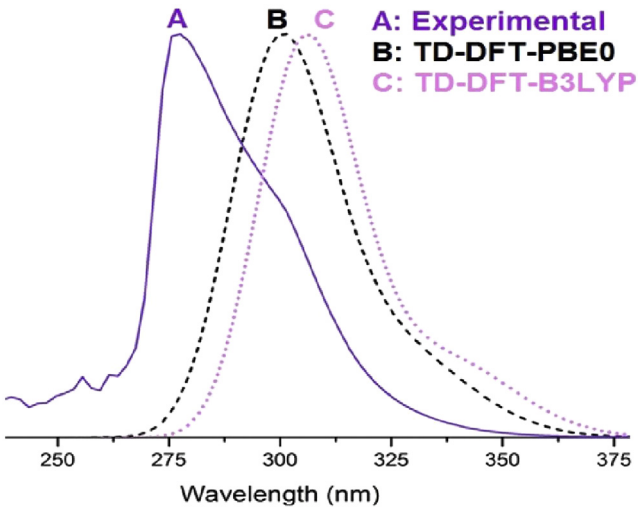

Fig. 5. Experimental (violet line) and theoretical PBE (black dashed line)/B3LYP (pink dashed line) UV–vis spectra of 6. (For interpretation of the references to colour in this figure legend, the reader is referred to the web version of this article.)

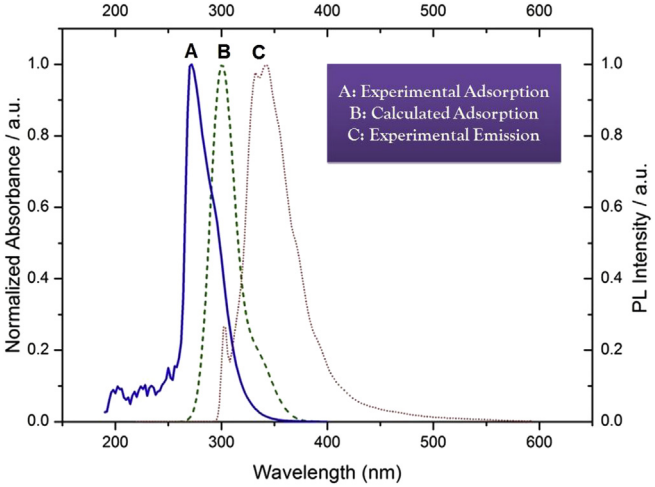

Fig. 4. Experimental absorption and experimental emission concentration at 2.7×10^{-4} M and theoretical (TD-DFT, PBE0/6–31++G**) absorption spectra of 9-(2-hydroxy-4,4-dimethyl-6-oxocyclohex-1-enyl)-3,3,dimethyl-2,3,4,9-tetrahydro-1*H*-xanthen-1-one.

clear from Fig. S4, the C–O and C–*O*–C groups represent the deep and soft red color zones, respectively, standing for the negative potential nature of these areas. The central zone of ring A represents a slight yellow color corresponding to a negligible negative potential. Other meaningful color zone is observed over the ring D, where there is a blue color zone. The Mulliken partial charges for all atoms of **6** obtained from DFT calculations in vacuum and in ethanol are reported in Supplementary Information section, Table S2. As it is predicted, the O atoms have gained negative charges as O4 (−0.198) > O3 (−0.123) > O2 (−0.108) > O1 (−0.073). Almost all C atoms were negatively charged, except for C1, C6, C7, C8, and C16, which is due to having α and β positions toward Oxygen-containing groups, and C11 and C19 because of a uniform distribution of electrons in these atoms. Moreover, all of the H atoms have positive partial charges as expected. Electron rich and electron poor position of compound 6 is appreciably confirmed by the results of Milliken population analysis.

3.7. *Vibrational analysis of* ***6***

The vibrational frequencies of **6** was calculated using DFT at the B3LYP and PBE0 functionals and 6–311++G** basis set and then compared with those obtained experimentally by FT-IR spectroscopy. Experimental and theoretical studies of **6** were provided in Fig. 7 and Table 5, respectively. In this investigation, the scaling factor employed from the B3LYP and PBE functionals are with values in the range of 0.97–1.02 [51].

The heteroaromatic and aromatic hydrocarbon structures show the presence of C–H stretching vibrations in the region 3000-3100 cm^{-1} by FT-IR spectrum [40,45]. In this region, the bands are not appreciably affected by the nature of the substituents. In the FT-IR spectrum, the bands at 3100, 2954, and 2874 cm^{-1} are assigned to the C–H stretching and the bands at 1440, 1376, 1311, 755, and 473 cm^{-1} are assigned to the C–H bending. The theoretical vibrations assigned to aromatic C–H stretching appear in the region 3100-3016 cm^{-1}, which is in agreement with the corresponding experimental values of 3088–3016 cm^{-1} previously reported for this kind of vibration [52,53]. While in case of our study, the C–H vibration frequencies appear at 3079 and 3111 by B3LYP functional and 3219 and 3247 cm^{-1} by PBE functional. The C–H symmetry stretching was observed at 3085 cm^{-1} with predicted bands at 3079 and 3111 cm^{-1} by B3LYP and PBE functionals, respectively. A medium C–H stretching vibration was observed at 2954 cm^{-1} and it is almost well correlated with the experimental value of 3016 cm^{-1}. In Table 5, FT-IR spectrum displayed the presence of aromatic ring (1643 cm^{-1}) and aliphatic hydrogen's (2980 cm^{-1}), which is close to the obtained results by Ghoran and co-workers [54]. C–H methyl bending vibrations were observed at 1376 cm^{-1} and it coincides with the computed value at 1392 cm^{-1}. A weak C–H in-plane bending vibration was observed at 1440 cm^{-1} and it exactly coincides with the calculated at ≈1440 cm^{-1}. With a medium intensity C–H bending vibrations was observed at 1312, 1257, 755 and 473 cm^{-1}, which correlated well with the predicted values 1320, 1248, 768 (out of plane), and 408 cm^{-1}, respectively. The experimental O–H vibrations have a much lower frequency

Table 3
TD-DFT energies (B3LYP and PBE0) and intensities of vertical excitations calculated for 9-(2-hydroxy-4,4-dimethyl-6-oxocyclohex-1-enyl)-3,3,dimethyl-2,3,4,9-tetrahydro-1H-xanthen-1-one and the corresponding composition in terms of one-electron transitions between molecularorbitals (H = HOMO and L = LUMO).

	Wavelength/nm	Oscillator Strength	Major Contributions
B3LYP (Vacuum)	301	0.073	H → L+1 (%30) and H → L (%27) and H-3 → L (%17)
	325	0.001	H-1 → L (%52) and H-1 → L+1 (%21)
	345	0.007	H → L (%71) and H → L+1 (%11)
B3LYP (Ethanol)	300	0.105	H → L (%27) and H → L+1 (%45)
	318	0.003	H-3 → L (%16), H-2 → L (%14) and H-1 → L (%48)
	334	0.017	H → L (%71) and H → L+1 (%15)
PBE0 (Vacuum)	300	0.105	H → L (62%) and H → L+1 (12%)
	318	0.003	H-2 → L (10%), H-1 → L (45%) and H-1 → L+1 (20%)
	334	0.017	H-3 → L (14%), H → L (36%) and H → L+1(26%)
PBE0 (Ethanol)	294	0.195	H → L (68%) and H → L+1 (12%)
	309	0.004	H-3 → L (20%), H-2 → L (25%) and H-1 → L (30%)
	324	0.034	H → L (30%), H → L+1 (38%) and H-3 → LUMO (9%)

Table 4
Frontier molecular orbitals and quantum molecular descriptors of 9-(2-hydroxy-4,4-dimethyl-6-oxocyclohex-1-enyl)-3,3,dimethyl-2,3,4,9-tetrahydro-1*H*-xanthen-1-oneat B3LYP and PBE0 methods.

Property	HOMO/eV	LUMO/eV	E_g/eV	μ/eV	η/eV	ω/eV	S/eV
B3LYP (Vacuum)	−5.92	−1.44	4.48	−3.68	2.24	3.03	0.223
B3LYP (Ethanol)	−5.80	−1.28	4.52	−3.54	2.26	2.80	0.221
PBE0 (Vacuum)	−6.10	−1.23	4.87	−3.66	2.44	2.25	0.205
PBE0 (Ethanol)	−6.39	−1.46	4.93	−3.93	2.46	3.14	0.203

(3178 cm^{-1}) when compared with the DFT ones (2746 and 2768 cm^{-1} at B3LYP and PBE methods, respectively). This is due to hydrogen bonding involving the hydroxyl groups taking place in the solid state, which is well-known to weaken O–H stretching vibrations, therefore decreasing the corresponding frequency [55–58]. Since the DFT calculations were done for one single molecule of **6** and without any explicit solvent molecules, no hydrogen bonding involving O–H groups takes place, which means O–H vibrations are stronger and have higher frequencies, as indeed observed. The ring C–C stretching bonds available in benzene causes six C–C stretching vibrations. The observed bands at 1589 and 1489 cm^{-1} in FT-IR are recognized as C=C double bond stretching vibrations. In Table 5, the experimental spectrum shows a strong band at around 1643 cm^{-1} is assigned to C–C stretching vibration which is comparable with the values of 1639 and 1652 cm^{-1} by B3LYP and PBE functionals, respectively [59]. The ring breathing mode is assigned at 589 and 1489 cm^{-1} in FT-IR. The calculated value at 1632 and 1512 cm^{-1} is in good agreement with experimental data. Moreover, the bands at 1704, 1697, 1673, 1643, 1535 are related to the C=C stretching mode of ring C and D which these results are appreciably supported by theoretical values for bands at B3LYP and PBE methods (see Table 5). Generally, C–O bands are displayed in the region 1205-1050 cm^{-1}. In the spectra of aliphatic ether bonds, the most characteristic absorption is a strong

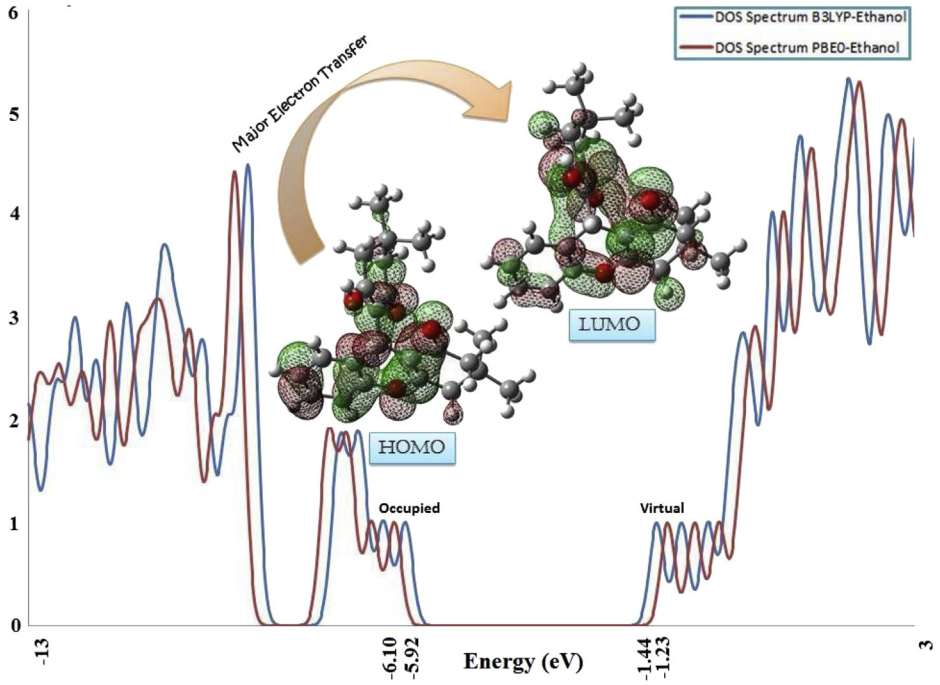

Fig. 6. DFT electron densities of the frontier molecular orbitals of 9-(2-hydroxy-4,4-dimethyl-6-oxocyclohex-1-enyl)-3,3,dimethyl-2,3,4,9-tetrahydro-1*H*-xanthen-1-oneoptimized in vacuum represented over the density of states (DOS) plot in ethanol phase at B3LYP and PBE0 methods and 6–311++G** basis sets.

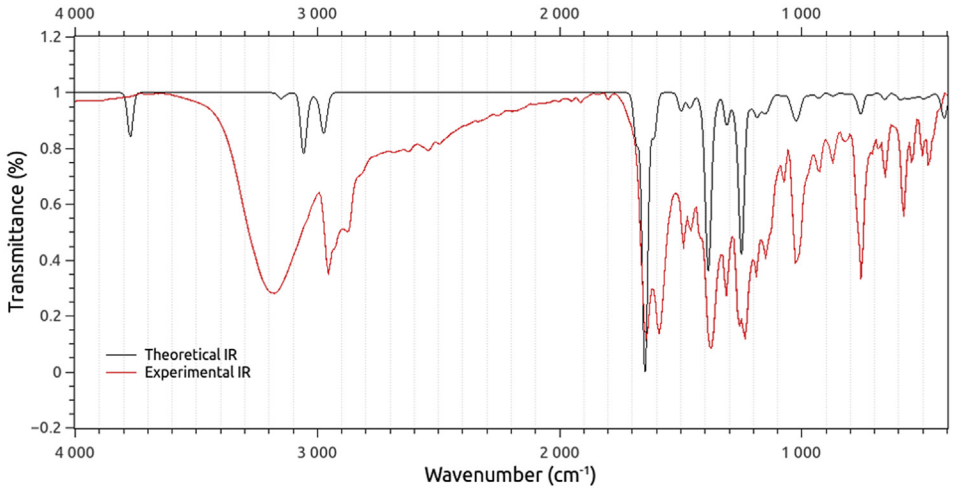

Fig. 7. Normalized experimental (FT-IR) and calculated (B3LYP/6–31++G**) infrared spectra of 9-(2-hydroxy-4,4-dimethyl-6-oxocyclohex-1-enyl)-3,3,dimethyl-2,3,4,9-tetrahydro-1*H*-xanthen-1-one.

band in the range of 1150–1085 cm^{-1}. Spectra of aryl alkyl ethers display an asymmetrical C–*O*–C stretching band at 1275-1200 cm^{-1} with symmetrical stretching near 1075-1020 cm^{-1}. In title molecule, the C–O stretching vibration is observed at 1200 and 1021 cm^{-1} and it exactly coincides with the calculated at 1200 and 1016 cm^{-1}. Moreover band at 1257 displays the C–*O*–C vibration of the xanthen ring (ring B) which is in good agreement with the results obtained by B3LYP (1278 cm^{-1}) and PBE (1279 cm^{-1}) methods. For more information of some selected modes calculated using potential energy distribution at B3LYP and PBE methods please see Table 5.

3.8. Raman spectroscopy study of **6**

The Raman spectroscopy has been implemented to plot the Raman spectra of **6** at excitation wavelength of 532 nm that is represented in Fig. 8. The in-plane stretching and deformation modes are represented by υ and δ. The band at 3435 cm^{-1} associates to the –OH group of ring D. The weak and medium strong bands at 1264, 1377 cm^{-1} and strong band at 2893 assign to $\delta(C-CH_3)$ vibrations and band at 1461 cm^{-1} represents the $\delta(CH_2)$ and $\delta(CH_3)$ asymmetric vibrations. Bands with weak intensities at 959 and 1132 cm^{-1} assign to the symmetric and asymmetric υ (C–*O*–C) vibrations and strong band at 1613 cm^{-1} relates to the hetero ring (xanthene ring). The band at 1027 cm^{-1}, and shoulder at 1508 cm^{-1} correspond to the υ (C–C) aromatic ring chain vibrations.

3.9. Nonlinear optical (NLO) analysis of **6**

As the final stage of our calculations, to measure Dipole Moment (DM), the linear polarizability (α) and the first hyperpolarizability (β) at the same DFT levels of theory as previously described, the corresponding values were inserted into the following equations [60]:

$$\text{Total Dipole Moment (Debye)} = DM_{X\text{direction}} + DM_{Y\ \text{direction}} + DM_{Z\ \text{direction}} \quad (1)$$

$$\alpha_{tot} = \left|\frac{\alpha_{xx} + \alpha_{yy} + \alpha_{zz}}{3}\right| \quad (2)$$

$$\beta tot = \sqrt{(\beta xxx + \beta xyy + \beta xzz)^2 + (\beta yyy + \beta yzz + \beta yxx)^2 + (\beta zzz + \beta zxx + \beta zyy)^2} \quad (3)$$

The result indicated that, the values of dipole moment, linear polarizability and first hyperpolarizability were 2.626 (Debye), 22.754 × 10^{-24}(esu) and 61.248 × 10^{-32} (esu) using B3LYP method. Ahmed et al. have reported the value of 20.3 × $10^{-24}$for the polarizability of 9H- xanthene compound which is in well agreement with our result [61].

4. Conclusions

New xanthene derivatives were synthesized from the reaction of dimedone with salicylaldehyde and its derivatives. Our alternative synthetic route is cheap, gives rise to high yields (75–85%) and does not use catalysts, making it very attractive. The synthesized xanthenes were characterized by state-of-the-art techniques and a single crystal of **6** could be grown and was analyzed by X-ray crystallography. Hirshfeld surface analysis revealed that most of the close contact interactions in the crystal involved hydrogens, which had a very high contribution (66.1%). The DFT calculations gave insight on the general properties of **6** and helped characterize that compound. The theoretical results also suggest that the functional B3LYP may be only employed for xanthene dyes when ground-state

Table 5
Selected vibrational assignments of 9-(2-hydroxy-4,4-dimethyl-6-oxocyclohex-1-enyl)-3,3,dimethyl-2,3,4,9-tetrahydro-1*H*-xanthen-1-oneby B3LYP and PBE methods.

R	Exp. Freq	B3LYP/6-31G(d,p)			PBE0/6-31G(d,p)			Characterization of normal modes with PED (%)
	FT-IR	Uns	S	I^{IR}	Uns	S	I^{IR}	
1	3178	3746.37	3746	67.48	3768.50	3769	84.04	**B**: υ OH Ring D (100) **P**: υ OH Ring D (100)
2	3224	3219.19	3219	13.46	3247.29	3247	8.99	**B**: υ_{sym} CH Ring A (97) **P**: υ_{sym} CH Ring A (94)
3	3209	3206.71	3207	27.87	3235.29	3235	20.66	**B**: υ_{sym} CH Ring A (99) **P**: υ_{sym} CH Ring A (99)
4	3193	3193.90	3194	10.80	3222.24	3222	7.89	**B**:υ_{sym} CH Ring A (98) **P**: υ_{sym} CH Ring A (93)
5	3185	3182.62	3183	0.94	3210.93	3211	0.92	**B**: υ_{sym} CH Ring A (98) **P**: υ_{sym} CH Ring A (90)
6	3108	3102.67	3103	14.70	3135.27	3135	14.70	**B**: υ CH [CH_2 and CH_3 Ring D] (87) **P**: υ CH [CH_2 and CH_3 Ring D] (91)
7	3100	3100.31	3100	6.50	3133.54	3134	7.30	**B**: υ CH [CH_2 and CH_3 Ring D] (80) **P**: υ CH [CH_2 and CH_3 Ring D] (97)
8	3093	3098.85	3099	5.90	3131.56	3132	5.84	**B**: υ CH [CH_2 Ring C] (81) **P**: υ CH [CH_2 Ring C] (99)
9	3085	3079.40	3079	1.60	3111.71	3112	6.20	**B**: υ CH [CH_2 Ring C] (90) **P**: υ CH [CH_2 Ring C] (99)
10	3085	3079.40	3079	1.60	3110.91	3111	1.79	**B**: υ_{chiral} CH xanthene Ring B (97) **P**: υ_{chiral} CH xanthene Ring B (99)
11	3031	3030.30	3030	16.41	3065.89	3066	11.99	**B**: υ CH [CH_2 Ring D] (97) **P**: υ CH [CH_2 Ring D] (98)
12	3023	3018.59	3019	14.04	3047.65	3048	11.73	**B**: υ CH [CH_2 Ring D] (98) **P**: υ CH [CH_2 Ring D] (89)
13	3016	3014.55	3015	15.69	3043.83	3044	15.26	**B**: υ CH [CH_2 Ring C] (85) **P**: υ CH [CH_2 Ring C] (98)
14	3008	3000.10	3000	36.95	3026.80	3027	31.53	**B**: υ CH [CH_2 Ring D] (99) **P**: υ CH [CH_2 Ring D] (97)
15	1743	1741.05	1741	16.14	1752.30	1752	302.94	**B**: υ sOC [CH_2 Ring C and D] (84) **P**: υ sOC [CH_2Ring C and D] (89)
16	1735	1732.25	1732	14.04	1743.40	1743	21.21	**B**: υ sOC [CH_2 Ring C and D] (78) **P**: υ sOC [CH_2Ring C and D] (80)
17	1704	1706.01	1706	65.41	1721.01	1721	65.80	**B**: υ sCC [C═C Ring C and D, C–C Aromaric Ring A] (39) **P**: υsCC [C═C Ring C and D, C–C Aromaric Ring A] (58)
18	1697	1695.08	1695	308.66	1711.27	1711	61.12	**B**: υ sCC [C═C Ring C and D, C–C Aromaric Ring A] (49) **P**: υ sCC [C═C Ring C and D, C–C Aromaric Ring A] (50)
19	1673	1670.29	1670	1.29	1682.64	1683	1.22	**B**: υ sCC [C═C Ring C and D, C–C Aromaric Ring A] (51) **P**: υ sCC [C═C Ring C and D, C–C Aromaric Ring A] (32)
20	1643	1639.18	1639	52.40	1651.84	1652	54.21	**B**: υ sCC [C═C Ring C and D, C–C Aromaric Ring A] (43) **P**: υ sCC [C═C Ring C and D, C–C Aromaric Ring A] (79)
21	1535	1539.37	1539	64.16	1540.84	1541	20.11	**B**: υ sCC [C═C Ring C and D, C–C Aromaric Ring A] (34) **P**: υ sCC [C═C Ring C and D, C–C Aromaric Ring A] (49)
22	1488	1487.20	1487	1.57	1477.90	1478	1.96	**B**: υ bHCH [H–C–H Ring C] (82) **P**: υ bHCH [H–C–H Ring C] (78)
23	1311	1361.49	1361	9.18	1377.47	1377	8.95	**B**: υ sCC [C═C Ring C and D, C–C Aromaric Ring A] (44) **P**: υ sCC [C═C Ring C and D, C–C Aromaric Ring A] (23)
24	1257	1278.82	1279	377.59	1279.03	1279	359.49	**B**: υ sCC [C–*O*–C xanthene Ring B] (29) **P**: υ sCC [C–*O*–C xanthene Ring B] (31)
25	1072	1067.66	1068	11.63	1069.76	1070	11.36	**B**: υ sCC [C═C Ring C and D, C–C Ring A] (62) **P**: υ sCC [C═C Ring C and D, C–C Ring A] (62)
26	964	963.50	963	0.49	959.09	959	0.53	**B**: υ sCC and HCCC [C–C and H–C–C–C of Ring] (77) **P**: υ sCC and HCCC [C–C and H–C–C–C of Ring] (61)

Abbreviations: Experimental (Exp), Frequency (Freq), Unscaled (Uns), Scaled (S), Infrared Intensity (I^{IR}), B3LYP (B), PBE (P).

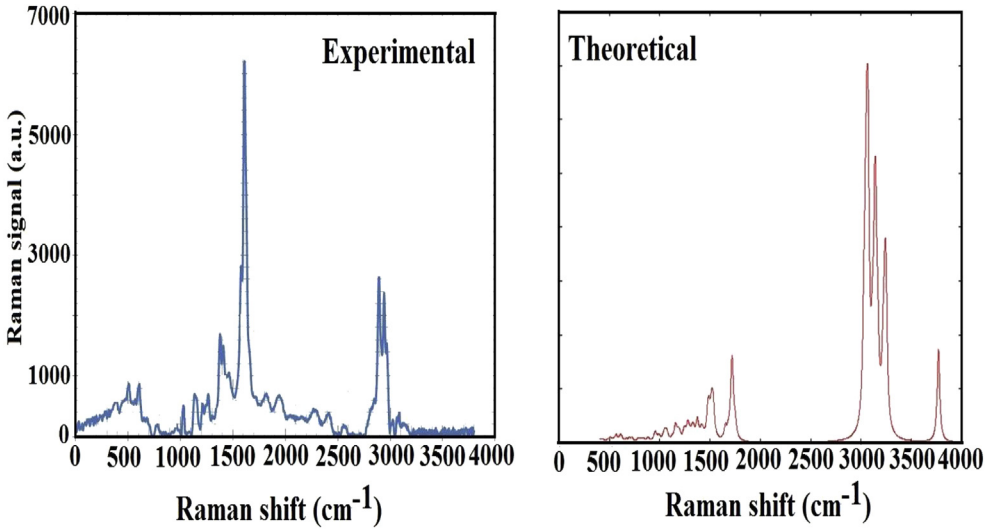

Fig. 8. Raman spectrum of 9-(2-hydroxy-4,4-dimethyl-6-oxocyclohex-1-enyl)-3,3,dimethyl-2,3,4,9-tetrahydro-1*H*-xanthen-1-one.

properties are envisaged, while PBE0 should be preferred when the prediction of excited-state properties is pursued. Comparison of the experimentally obtained and theoretical predicted IR bands and UV–Vis absorption spectra were appreciably similar. The bands observed at Raman spectroscopy study confirm the formation of 6 where the C–H, C–*O*–C, C–C and O–H bands are clearly visible in the Raman spectrum.

Acknowledgments

The authors want to thank Urmia University for providing partial support of the work and instrumental analysis facilities.

Appendix A. Supplementary data

Supplementary data related to this article can be found at http://dx.doi.org/10.1016/j.molstruc.2017.08.054.

References

[1] X.J. Liu, M. Zhang, M.P. Yang, B. Li, Z. Cheng, B.Q. Yang, Tetrahedron 71 (2005) 8194.
[2] E.C. Horning, M.G. Horning, J. Org. Chem. 11 (1946) 95.
[3] N. Sato, M. Jitsuoka, T. Shibata, T. Hirohashi, K. Nonoshita, M. Moriya, Y. Haga, A. Sakuraba, M. Ando, T. Ohe, H. Iwaasa, A. Gomori, A. Ishihara, A. Kanatani, T. Fukami, J. Med. Chem. 51 (2008) 4765.
[4] J.M. Jamison, K. Krabill, A. Hatwalkar, Cell. Biol. Int. Rep. 14 (1990) 1075.
[5] A.M. El-Brashy, M.M. El-Sayed, F.A. El-Sepai, II Farm. 59 (2004) 809.
[6] P.V. Murphy, J.L. O'Brien, L.J. Gorey-Feret, A.B. Smith, Tetrahedron 59 (2003) 2259.
[7] H. Wu, X. Chen, Y. Wan, H. Xin, H. Xu, C. Yue, L. Pang, R. Ma, Synth. Commun. 21 (2009) 3762.
[8] C.G. Knight, T. Stephens, Biochem. J. 258 (1989) 683.
[9] A.K. Bhattacharya, K.C. Rana, M. Mujahid, I. Sehar, A.K. SaxenaBioorg, Med. Chem. Lett. 19 (2009) 5590.
[10] X.Z. Wang, B.Y. Yang, G.J. Lin, Y.Y. Xie, H.L. Huang, Y.J. Liu, DNA Cell. Biol. 31 (2012) 1468.
[11] A. Ilangovan, K. Anandhan, M.P. Kaushik, P. Vijayakumar, R. Renganathan, D.A. Ananth, T. Sivasudha, Med. Chem. Res. 24 (2015) 344.
[12] Y. Yang, J.O. Escobedo, A. Wong, C.M. Schowalter, M.C. Touchy, L. Jiao, W.E. Crowe, F.R. Fronczek, R.M. Strongin, J. Org. Chem. 70 (2005) 6907.
[13] J.V. McCullagh, K.A. Daggett, J. Chem. Educ. 84 (2007) 1799.
[14] P. Pradeep, J.S. Rao, J. Shubha, Res. J. Chem. Sci. 2 (2012) 21.
[15] K.V. Sashidhara, A. Kumar, R.P. Dodda, B. Kumar, Tetrahedron. Lett. 53 (2012) 3281.
[16] A.S. Gazizov, A.V. Smolobochkin, J.K. Voronina, A.R. Burilov, M.A. Pudovik, Tetrahedron 71 (2015) 445.
[17] B.A. Shainyan, S.V. Kirpichenko, E. Kleinpeter, S.A. Shlykov, D.Y. Osadchiy, Tetrahedron 71 (2015) 3810.
[18] M.L. Roldán, A.E. Ledesma, A.B. Raschi, M.V. Castillo, E. Romano, S.A. Brandán, J. Mol. Struct. 1041 (2013) 73.
[19] B. Sjöberg, S. Foley, B. Cardey, M. Enescu, Spectrochim. Acta. A. 128 (2014) 300.
[20] J.M. Ramos, M.T.M. Cruz, A.C. Costa Jr., G.F. Ondar, G.B. Ferreira, L. Raniero, A.A. Martin, O. Versiane, C.A. Tellez Soto, Spectrochim. Acta. A. 97 (2012) 1041.
[21] S. Sebastian, S. Sylvestre, N. Sundaraganesan, M. Amalanathan, S. Ayyapan, K. Oudayakumar, B. Karthikeyan, Spectrochim. Acta. A. 107 (2013) 167.
[22] A. Ouasria, F. Lambarkia, A. Rhandoura, TsK. Zaharievc, N. Trendafilovac, I. Georgieva, Vib. Spectrosc. 88 (2017) 83.
[23] V.L. Furera, A.E. Vandyukovb, J.P. Majoralc, A.M. Caminadec, V.I. Kovalenko, Vib. Spectrosc. 88 (2017) 14.
[24] E. Bartoszak-Adamska, Z. Dega-Szafran, A. Komasa, M. Szafran, Vib. Spectrosc. 88 (2017) 106.
[25] A. R. Katritzkyfrs, Academic Press, New York, 1983, pp. 34.
[26] L. Jurd, J. Org. Chem. 31 (1966) 1639–1641.
[27] Y.L. Li, X.S. Wang, D.Q. Shi, S.J. Tu, Y. Zhang, Acta. Crystallogr. Sect. e. 60 (2004) O1439.
[28] M.J. Frisch, G.W. Trucks, H.B. Schlegel, G.E. Scuseria, M.A. Robb, J.R. Cheeseman, G. Scalmani, V. Barone, B. Mennucci, G.A. Petersson, H. Nakatsuji, M. Caricato, X. Li, H.P. Hratchian, A.F. Izmaylov, J. Bloino, G. Zheng, J.L. Sonnenberg, M. Hada, M. Ehara, K. Toyota, R. Fukuda, J. Hasegawa, M. Ishida, T. Nakajima, Y. Honda, O. Kitao, H. Nakai, T. Vreven, J.A. Montgomery Jr., J.E. Peralta, F. Ogliaro, M. Bearpark, J.J. Heyd, E. Brothers, K.N. Kudin, V.N. Staroverov, R. Kobayashi, J. Normand, K. Raghavachari, A. Rendell, J.C. Burant, S.S. Iyengar, J. Tomasi, M. Cossi, N. Rega, J.M. Millam, M. Klene, J.E. Knox, J.B. Cross, V. Bakken, C. Adamo, J. Jaramillo, R. Gomperts, R.E. Stratmann, O. Yazyev, A.J. Austin, R. Cammi, C. Pomelli, J.W. Ochterski, R.L. Martin, K. Morokuma, V.G. Zakrzewski, G.A. Voth, P. Salvador, J.J. Dannenberg, S. Dapprich, A.D. Daniels, Ö. Farkas, J.B. Foresman, J.V. Ortiz, J. Cioslowski, D.J. Fox, Gaussian, Inc, Wallingford CT, 2009.
[29] M.H. Jamroz, Vibrational Energy Distribution Analysis VEDA 4, Warsaw, 2004-2010.
[30] S.K. Wolff, D.J. Grimwood, J.J. McKinnon, M.J. Turner, D. Jayatilaka, M.A. Spackman, Crystal Explorer (Version 3.0), University of Western Australia, 2012.
[31] G. Gilli, P. Gilli, J. Mol. Struct. 552 (2000) 1.
[32] P. Gilli, G. Gilli, J. Mol. Struct. 972 (2010) 2.
[33] B.J. Emsley, Prog. Inorg. Chem. 9 (1968) 161.
[34] Melvin D. Joesten, J. Chem. Edu. 59 (1982) 362.
[35] J.C. Wallet, E. Molins, C. Miravitlles, J. Phys. Org. Chem. 11 (1998) 751.
[36] J.C. Wallet, E. Molins, C. Miravitlles, Struct. Chem. 11 (2000) 319.
[37] A.H. Dabbagh, N. Noroozi Pesyan, B.O. Patrick, B.R. James, Can. J. Chem. 82 (2004) 1179.
[38] V.R. Batistela, D.S. Pellosi, F.D. de Souza, W.F. da Costa, Santin S.M. de Oliveira, V.R. de Souza, W. Caetano, H.P.M. de Oliveira, I.S. Scarminio, N. Hioka, Spectrochim. Acta. Sect. A 79 (2011) 889.
[39] N. Noroozi Pesyan, M. Jalilzadeh, N. Yalabi Torkaman, E. Şahin, J. Iran. Chem. Soc. 11 (2014) 35.
[40] M.S. Boobalan, M. Amaladasan, D. Tamilvendan, S. Ramalingam, G.V. Prabhu, Spectrochim. Acta. A. 131 (2014) 303.
[41] K. Anandhan, M.S. Boobalan, P. Venkatesan, A. Ilangovan, M.P. Kaushik, C. Arunagiri, J. Mol. Struct. 1097 (2015) 185.
[42] K.H. Drexhage, J. Res. Natl. Bur. Stand. A. Phys. Chem. 3 (1976).
[43] M. Sibrian-Vazquez, J.O. Escobedo, M. Lowry, F.R. Fronczek, R.M. Strongin,

J. Am. Chem. Soc. 134 (2012) 10502.
[44] Y. Yang, M. Lowry, X. Xu, J.O. Escobedo, M. Sibrian-Vazquez, L. Wong, C.M. Schowalter, T.J. Jensen, F.R. Fronczek, I.M. Warner, R.M. Strongin, PNAS 105 (2008) 8829.
[45] T. Yempala, B. Sridher, S. Kantevari, J. Chem. Sci. 127 (2015) 803.
[46] H. Moghanian, A. Mobinikhaledi, R. Monjezi, Des. Monomers Polym. 18 (2014) 157.
[47] T. Koopmans, Physica 1 (1934) 104.
[48] J.C. Phillips, Phys. Rev. 123 (1961) 420.
[49] J.S. Murray, K. Sen, Molecular Electrostatic Potentials: Concepts and Applications, Elsevier, Amsterdam, 1996.
[50] E. Scrocco, J. Tomasi, in: P. Lowdin (Ed.), Advances in Quantum Chemistry, Academic Press, New York, NY, USA,, 1978.
[51] A.P. Scott, L. Radom, J. Phys. Chem. 100 (1996) 16502–16513.
[52] J. Coates, Interpretation of Infrared Spectra, a Practical Approach, John Wiley and Sons Ltd., Chichester, 2000.
[53] G. Varsanyi, L. Lang, Adam Hilger, Vibrational Spectra of Benzene Derivatives, London, 1974.
[54] S.H. Ghoran, V. Atabaki, E. Babaei, S.R. Olfatkhah, M. Dusek, V. Eigner, A. Soltani, A.D. Khalaji, Bioorg. Chem. 66 (2016) 27.
[55] R.M. Silverstein, G.C. Bassler, T.C.Morrill, John Wiley & Sons, New York, 1991.
[56] P. Leyton, C. Paipa, A. Berrios, A.Z. Rate, S. Fuentes, M.V. Castillo, S.A. Brandán, J. Mol. Struct. 1031 (2013) 110.
[57] Stoe&Cie GmbH, X-AREA, Version 1.31, Stoe&Cie GmbH, Darmstadt, Germany, 2005.
[58] G.M. Sheldrick, SHELXS97 and SHELXL97, University of Göttingen,Germany, 1997.
[59] G. Varsanyi, Assignments for Vibrational Spectra of Sven Hundred Benzene Derivatives, vols. 1–2, Academic Kiado, Budapest, 1973.
[60] M. Dadsetani, A.R. Omidi, J. Phys. Chem. C 119 (2015) 16263.
[61] S.A. Ahmed, N.O. Obi-Egbedi, I. Iweibo, Phys. Chem. 2 (2012) 16.